Boundary Layer Stability and Transition in a Chemically Reacting Martian Atmosphere using LASTRAC

H.L. Kline*
National Institute of Aerospace, Hampton, VA, 23666

C.-L. Chang† and F. Li‡
NASA Langley Research Center, Hampton, VA, 23681

The Thermal Protection System (TPS) is a significant portion of the mass of reentry vehicles, planetary probes, and Martian entry vehicles. Reducing this mass has benefits in terms of decreased fuel requirements and increased payload; however, due to the high risk and uncertainty, the TPS or heat shields are designed conservatively by assuming fully turbulent flow. Laminar flow results in reduced heat flux, and improved transition prediction has the potential to reduce TPS mass and uncertainty in aerothermodynamic predictions. Limited previous research exists examining the problem of transition prediction for Martian atmospheric entry, with studies available on transition on the Mars Science Laboratory TPS. Although transition was demonstrated in wind-tunnel tests, uncertainty in the transition location resulted in a TPS designed for fully turbulent flow, and therefore greater mass than required for a partially-laminar condition. In this work, we extend the boundary layer stability code LASTRAC, recently modified to include chemical and thermal nonequilibrium capabilities, to a model of the Martian atmosphere. LASTRAC provides Parabolized Stability Equations (PSE) as well as Linear Stability Theory (LST) to predict the stability of a boundary layer and transition with semi-empirical e^N methods. Results included in this work compare disturbance growth characteristics between air and Martian atmosphere at similar nondimensional freestream conditions on a simple flat plate geometry. Both chemical nonequilibrium and thermochemical nonequilibrium, as well as both PSE and LST, are used.

I. Nomenclature

ρ	=	density [kg m^{-3}]
p	=	pressure [Pa]
T	=	temperature [K]
e	=	energy per unit mass [J kg^{-1}]
h	=	enthalpy per unit mass [J kg^{-1}]
C_s	=	mass fraction for species s
k	=	thermal conductivity [J m^{-1}s^{-1}K^{-1}]
μ	=	viscosity [N s m^{-2}]
ν	=	dynamic viscosity [kg s^{-1} m^{-1}]
λ	=	2nd viscous coefficient [N s m^{-2}]
t	=	time [s]
f	=	frequency [Hz]
ℓ	=	boundary layer length scale [m]
x, y, z	=	body-fitted coordinates
h_1, h_3	=	curvature terms
$\vec{V}$	=	velocity vector [m/s]
M_s	=	molar mass for species s [g]
m_s	=	particle mass for species s [g]

*Research Engineer, Research Department, MS 128, AIAA Member.
†Aerospace Technologist, Computational Aerosciences Branch, MS 128, Associate Fellow, AIAA.
‡Aerospace Technologist, Computational Aerosciences Branch, MS 128.

γ_s	=	molar concentration for species s
$\alpha_{s,r}$, $\beta_{s,r}$	=	stoichiometric coefficients
$R_{f,r}$, $R_{b,r}$	=	forward and backward reaction rates
τ_s	=	vibrational-translational relaxation time [s]
$\dot{\omega}_s$	=	species production rate [kg m^{-3} s^{-1}]
D_{sr}	=	diffusion coefficient of species s with respect to species r [$m^2 s^{-1}$]
D_s	=	diffusion coefficient of species s with respect to the mixture [$m^2 s^{-1}$]
C_p, C_v	=	constant pressure and constant volume specific heats [J $mol^{-1} K^{-1}$]
$C_{p,s}$, $C_{v,s}$	=	constant pressure and constant volume specific heats for species s [J $mol^{-1} K^{-1}$]
$C^s_{v,V}$	=	constant volume specific heat for vibrational energy for species s [J $mol^{-1} K^{-1}$]
γ	=	ratio of specific heats
S	=	entropy [J $mol^{-1} K^{-1}$]
$\pi\bar{\Omega}^{(1,1)}_{ij}$,$\pi\bar{\Omega}^{(2,2)}_{ij}$	=	collision integrals between species i and j [m^2]
$\Delta^{(1)}_{ij}$,$\Delta^{(2)}_{ij}$	=	modified collision integrals between species i and j [m s]
k_B	=	Boltzmann's constant [J K^{-1}]
Av	=	Avogadro's number [mol^{-1}]
R_u	=	universal gas constant [J $mol^{-1} K^{-1}$]
Re	=	Reynolds number
Re_u	=	unit Reynolds number [m^{-1}]
Le	=	Lewis number
Pr	=	Prandtl number
Ec	=	Eckert number
M	=	Mach number
F	=	nondimensionalized frequency
ϕ	=	disturbance vector
α_i	=	imaginary component of complex wave number α
$()_s$	=	species quantity
$()_e$	=	edge of boundary layer
$()_d$	=	dimensional quantity
$\bar{()}$	=	mean value
$()'$	=	disturbance value
$()_{el}$	=	electronic value
$()_V$	=	vibrational-electronic value
$()_{tr}$	=	translational-rotational value
FR	=	Finite-rate chemistry, chemical nonequilibrium and thermal equilibrium
TNE	=	Thermochemical Nonequilibrium

II. Introduction

Hypersonic boundary layer transition is critically important to hypersonic vehicle design due to its influence on heat transfer rates. Prediction of heat transfer informs the design of the Thermal Protection System (TPS), which is a significant portion of the mass of reentry vehicles, planetary probes, and Martian entry vehicles. Reducing this mass has benefits in terms of decreased fuel requirements and increased payload; however, due to the high risk and uncertainty, the TPS or heat shield is often designed conservatively assuming fully turbulent flow. Laminar flow results in reduced heat flux, and so more accurate and reliable prediction of transition should result in more efficient vehicle design. Limited previous research exists examining the problem of transition prediction for Martian atmospheric entry, with literature available on transition on the Mars Science Laboratory (MSL). Although transition was demonstrated in wind-tunnel tests [1], flight data [2], and numerical studies [3, 4], uncertainty in the transition location was held to be high enough that the TPS should be designed for fully turbulent flow, and therefore, greater mass than would have been required for a partially-laminar TPS design.

Although Mach number and Reynolds number based on momentum thickness are commonly used for developing correlations to predict transition points, and have been used in previous studies for Martian entry applications, these correlations require a significant amount of data in order to be developed, and there is a large degree of uncertainty in

applying such a correlation to situations outside of the specific wind tunnel or geometry used to gather the data. By contrast the Linear Stability Theory (LST), linear Parabolized Stability Equations (PSE), and Nonlinear PSE (NPSE) methods provide a physics-based analysis of the boundary layer stability. These e^N methods are semi-empirical due to requiring knowledge of the critical N-factor for transition onset, and in the case of NPSE the initial disturbance amplitude is required. Saric et al. [5] reviewed the instability mechanisms that lead to laminar-turbulent transition, which can be categorized as streamwise (Mack 1st and 2nd modes), crossflow, centrifugal (Görtler), and attachment-line. In this work, the focus is on the 2nd mode, which is dominant at high Mach numbers in the absence of crossflow. Predicting the exact point of transition is a difficult task that requires not only detailed analysis of boundary layers stability, but also detailed knowledge of the disturbances that will be encountered. Under most situations, the exact point of transition cannot be predicted due to a lack of knowledge about the freestream disturbances. The accepted practice is to reduce the N-factor of a vehicle design in order to delay transition and improve the performance through a reduction of the percentage of the surface impacted by turbulent flow, despite not knowing the exact point of transition.

Chemical and thermal nonequilibrium are relevant to reentry applications because under hypersonic conditions the temperature within the boundary layer and behind strong shocks can rise above the point where molecular dissociation and chemical reactions will occur. At high enough temperatures, ionization reactions are possible, and in the case of ablative Thermal Protection Systems (TPS), the ablating material may react with the surrounding atmosphere, with the reaction mechanism depending on the chemical composition of the material. In order to accurately model the aerodynamics and boundary layer stability of this system, the chemistry effects must be taken into account. The presence of transitional flow, and the difficulty of accurately predicting the point of transition, is a major source of uncertainty, particularly for predicting heating [6] for hypersonic vehicles. A number of analytical studies focusing on hypersonic boundary layer transition neglecting chemistry effects are available in the literature [3, 7–10], as well as experimental studies that use sufficiently low temperatures to avoid significant chemical reactions [11]. Relatively fewer studies exist that include chemistry effects are available [12–15]. Chemical equilibrium, chemical nonequilibrium or finite-rate chemistry, and thermochemical nonequilibrium have been compared in the past [16–19]. There are a number of recently-developed options for more advanced chemical models than will be addressed here, for example Jaffe et al. [20], Armenise et al. [21] and Chaudhry et al.[22]. The code used in this work has been developed with the intention of being compatible with any user-provided chemical model, and while further investigation on the effects of the chemical model are outside the scope of this work, it is has been shown that nonequilibrium chemistry is sensitive to the models used, and that boundary layer stability specifically is sensitive to vibrational energy relaxation as shown by Bertolotti[23] and touched on briefly in Figure 5 of Kline et al.[19].

Schneider[24] reviewed the available literature on laminar-turbulent transition for blunt body and capsule geometries, including Martian probe atmospheric entry, and MSL. In [24], Schneider discusses how transition over reentry shields is critical both for increasing the available payload through decreasing TPS thickness and for predicting and avoiding high, localized heating from aft-body boundary layer reattachment. Edquist et al.[25] conducted detailed computational studies of the MSL, focusing on thermal and chemical nonequilibrium with an eight-species gas mixture, using Park [26] reaction rates and using a critical value of momentum-thickness Reynolds number. The peak turbulent heating rate was predicted to be 70% higher than the heating rate for laminar flow, with a fully turbulent shield experiencing 38% higher integrated heat load as compared to the fully laminar case. Kimmel [27] provides a thorough review of hypersonic transition control techniques, and states that one of the difficulties of hypersonic transition control is that the techniques applied at lower speeds cannot be extrapolated to the high heating environment and the physical phenomena occurring within these boundary layers. At the same time, the potential benefits of a greater understanding of hypersonic boundary layer transition are significant. Analysis of the National AeroSpace Plane (NASP) aerodynamics [28] estimated that the possible payload of an air-breathing single-stage-to-orbit vehicle would double if it was fully laminar as compared to fully turbulent. Techniques to control transition include wall cooling, which is effective in stabilizing the first Mack mode but destabilizing to the 2nd mode [27, 29]. Hollis et al. [1] compared laminar, transitional, and turbulent heating data on the MSL entry vehicle in an air wind tunnel and a high-enthalpy shock tunnel with CO_2 gas, and compared results to Navier-Stokes solutions. Using laminar CFD solutions, they produced transition location correlations based on boundary layer momentum thickness, edge Mach number, and Reynolds number based on momentum thickness. Selected cases from these wind tunnel tests have been analyzed with the Langley Stability and Transition Analysis Code (LASTRAC) [30] by Chang et al.[3] with air only and PSE-Chem by Johnson et al.[4] using LST with a $CO_2 - N_2$ mixture and PSE analysis for air. Although not applied to Martian entry applications, experimental and computational work has been done investigating a stabilizing effect of CO_2 injection into high enthalpy boundary layers for delay of transition[31–33], due to the characteristic of CO_2 to absorb energy at frequencies close to the 2nd Mack mode.

In this work, we extend boundary layer instability with chemical and thermochemical nonequilibrium to a model of

the Martian atmosphere using LASTRAC [30] which is a boundary-layer stability analysis code that provides PSE as well as LST to predict the stability of a boundary layer and transition with semi-empirical e^N methods. The capability to address finite-rate chemistry as well as thermochemical nonequilibrium has recently been implemented for LASTRAC by Kline et al. [19]. The current work focuses on application of these methods to Martian atmospheric conditions on simple geometry, and results are compared to boundary layer stability in air.

III. Methodology

The Langley Stability and Transition Analysis Code (LASTRAC) has recently been modified to allow finite-rate (FR) chemistry in thermal equilibrium, chemical equilibrium, and thermochemical nonequilibrium (TNE) air gas chemistry. These capabilities are required for hypersonic boundary layer transition prediction since at the high temperatures experienced by hypersonic vehicles air can no longer be assumed a perfect gas, and the chemical and thermochemical nonequilibrium effects should be taken into account. In this work, we further extend this capability to Martian atmosphere gas chemistry. Section A will describe the Parabolized Stability Equations (PSE), followed by a description of the chemical model in Section B and mean flow solutions in Section C. In this work, "Martian" refers to an 8-species gas mixture of CO_2, N_2, O_2, NO, CO, C, O, and N with freestream conditions of 97% CO_2 and 3% N_2 by mass. "Earth" or "air" refers to a 5-species gas mixture of O_2, N_2, NO, N, and O, with freestream conditions of 21% O_2 and 79% N_2 by mass.

A. Boundary Layer Stability Analysis

LASTRAC includes capabilities to analyze boundary layer stability with LST and PSE. These methods assume a disturbance vector solution that is a discrete sum of a Fourier series. The LST method assumes that the boundary layer is nearly parallel, with negligible growth of the thickness of the boundary layer, and uses a mode shape for the Fourier series that has a shape function and wave number that are locally constant in the streamwise direction. For the PSE, the assumed mode shape uses a shape function and wave number that vary slowly in the streamwise direction. While an eigenvalue problem is formed in the LST approach, the PSE method numerically solves an approximate form of the governing partial differential equations for the slow-varying shape function with an actively updated wave number along the streamwise direction. The nonlinear PSE uses a mode shape similar to the PSE, but retains nonlinear terms from the Navier-Stokes equations, and requires a known finite disturbance while both LST and linear PSE are independent of the input disturbance amplitude but only valid for sufficiently small disturbances. LASTRAC was recently modified to include further capabilities for high-enthalpy hypersonic applications by Kline et al.[19]. Further details on the capabilities previously available in LASTRAC are available in the LASTRAC manual [30]. The methodology will be summarized here, with particular attention to various aspects that were modified to accommodate gas chemistry effects.

Stability equations are derived starting from the nondimensionalized Navier-Stokes equations,

$$\begin{aligned}
\frac{\partial \rho}{\partial t} + \nabla \cdot \left(\rho \vec{V}\right) &= 0 \\
\rho \left[\frac{\partial \vec{V}}{\partial t} + \left(\vec{V} \cdot \nabla\right) \vec{V}\right] &= -\nabla p + \frac{1}{Re}\left(\nabla[\lambda(\nabla \cdot \vec{V})] + \nabla \cdot [\mu(\nabla \vec{V} + \nabla \vec{V}^T)]\right) \\
\rho C_p \left[\frac{\partial T}{\partial t} + (\vec{V} \cdot \nabla) T\right] &= \frac{1}{RePr} \nabla \cdot (k \nabla T) + Ec\left(\frac{\partial p}{\partial t} + (\vec{V} \cdot \nabla) p\right) + Ec \frac{\Phi}{Re}\,.
\end{aligned} \tag{1}$$

For a calorically perfect gas,

$$\begin{aligned}
\Phi &= \lambda(\nabla \cdot \vec{V})^2 + \frac{\mu}{2}\left[\nabla \vec{V} + \nabla \vec{V}^T\right]^2 \\
\mu &= f(T), \quad \lambda = \frac{2}{3}(s-1)\mu \\
p &= \rho R T, \\
C_p &= const, \quad R = const,
\end{aligned} \tag{2}$$

where s is the Stokes parameter, μ is the viscosity, λ is the 2nd coefficient of viscosity, R is the gas constant, C_p is the specific heat at constant pressure, p is the pressure, ρ is the density, $\vec{V} = \{u, v, w\}$ is the velocity, and T is the temperature.

Nondimensional numbers that appear in the equations are: the Reynolds number, Lewis number, Prandtl number, Eckert number, and Mach number:

$$\begin{aligned} Re &= \frac{u_e \ell}{\nu_e}, \quad & Le &= \frac{\rho_e D_e C_{p,e}}{k_e}, \quad & Pr &= \frac{\mu_e C_{p,e}}{k_e}, \\ Ec &= \frac{u_e^2}{C_{p,e} T_e} \quad & &= (\gamma_e - 1) M_e^2, \quad & M_e &= \frac{|\vec{V}_e|}{\sqrt{\gamma_e R_e T_e}}, \end{aligned} \tag{3}$$

where all normalizing values are taken at the edge of the boundary layer. Equation 1 has been nondimensionalized with:

$$\begin{aligned} T &= T_d / T_e & \rho &= \rho_d / \rho_e & \vec{V} &= \vec{V}_d / u_e \\ p &= p_d / (\rho_e u_e^2) & \ell &= \sqrt{\nu_e x_d / u_e} & \mu &= \mu_d / \mu_e \\ x &= x_d / \ell & k &= k_d / k_e & C_p &= C_{p,d} / C_{p,e}\,, \end{aligned} \tag{4}$$

where the subscript e indicates the dimensional value at the edge of the boundary layer along the normal to the surface, and the subscript d indicates the local dimensional quantity. The quantity ℓ is the dimensional boundary layer length scale, and x_d is the dimensional coordinate in the streamwise direction. Quantities that have no subscript are nondimensional unless otherwise stated. We take the solution to be composed of the mean flow and a fluctuation,

$$\begin{aligned} u &= \bar{u} + u' & v &= \bar{v} + v' & w &= \bar{w} + w' \\ p &= \bar{p} + p' & \rho &= \bar{\rho} + \rho' & T &= \bar{T} + T' \\ \mu &= \bar{\mu} + \mu' & \lambda &= \bar{\lambda} + \lambda' & k &= \bar{k} + k', \end{aligned} \tag{5}$$

which is substituted into Equation 1. A body-fitted coordinate system will be used where x, y, and z are defined as streamwise, wall-normal, and spanwise, respectively. Element lengths are $h_1 dx$, dy, and $h_3 dz$, accounting for streamwise and transverse curvature in the x and z directions. Subtracting Equation 1 for the mean flow and stating the result in terms of Jacobians and the disturbance vector $\phi = \{p', u', v', w', T'\}^T$,

$$\begin{aligned} \Gamma \frac{\partial \phi}{\partial t} + \frac{A}{h_1}\frac{\partial \phi}{\partial x} + B\frac{\partial \phi}{\partial y} + C\frac{\partial \phi}{\partial z} + D\phi = \frac{1}{Re_0}\Bigg(& \frac{V_{xx}}{h_1^2}\frac{\partial^2 \phi}{\partial x^2} + \frac{V_{xy}}{h_1}\frac{\partial^2 \phi}{\partial x \partial y} + V_{yy}\frac{\partial^2 \phi}{\partial y^2} \\ & + \frac{V_{xz}}{h_3}\frac{\partial^2 \phi}{\partial x \partial z} + \frac{V_{yz}}{h_3}\frac{\partial^2 \phi}{\partial y \partial x} + \frac{V_{zz}}{h_3^2}\frac{\partial^2 \phi}{\partial z^2}\Bigg), \end{aligned} \tag{6}$$

where Γ, A, B, C, D, V_{xx}, V_{xy}, V_{xz}, V_{yz}, and V_{zz} are the Jacobians for this system, representing the dependence of the mass, momentum, and energy on the disturbances ϕ. Re is the Reynolds number, and $Re_0 = \frac{u_e \ell_0}{\nu_e}$, where ℓ_0 is the reference length scale, u_e is the boundary layer edge velocity, and ν_e is the kinematic viscosity at the boundary layer edge.

Since the Jacobians at this point depend on perturbed quantities, there are 2nd-order perturbations included in Equation 6. The linearized form is found by separating each Jacobian into two parts that respectively contain only mean flow quantities or only perturbation quantities, e.g., $A = \bar{A} + A'$. Because ϕ is a vector of perturbed quantities, the linearized form of these equations retains only the mean flow portion of the Jacobians,

$$\begin{aligned} \bar{\Gamma} \frac{\partial \phi}{\partial t} + \frac{\bar{A}}{h_1}\frac{\partial \phi}{\partial x} + \bar{B}\frac{\partial \phi}{\partial y} + \bar{C}\frac{\partial \phi}{\partial z} + \bar{D}\phi = \frac{1}{Re_0}\Bigg(& \frac{\bar{V}_{xx}}{h_1^2}\frac{\partial^2 \phi}{\partial x^2} + \frac{\bar{V}_{xy}}{h_1}\frac{\partial^2 \phi}{\partial x \partial y} + \bar{V}_{yy}\frac{\partial^2 \phi}{\partial y^2} \\ & + \frac{\bar{V}_{xz}}{h_3}\frac{\partial^2 \phi}{\partial x \partial z} + \frac{\bar{V}_{yz}}{h_3}\frac{\partial^2 \phi}{\partial y \partial x} + \frac{\bar{V}_{zz}}{h_3^2}\frac{\partial^2 \phi}{\partial z^2}\Bigg). \end{aligned} \tag{7}$$

The disturbance field ϕ is assumed to be periodic in space and time, and so the disturbance vector can be expressed as a Fourier series,

$$\phi(x, y, z, t) = \sum_{m=-M}^{M} \sum_{n=-N}^{N} \chi_{mn}(x, y) e^{i(n\beta z - m\omega t)}\,, \tag{8}$$

where M and N represent the numerical resolution in time and space, respectively. The fundamental temporal wave number is a nondimensionalized form of the physical frequency f, $\omega = \frac{2\pi\ell}{u_e} f$.

Substituting a single disturbance mode defined by the wave number $\omega = \frac{2\pi\ell}{u_e} f$ and spanwise wave number $\beta = \frac{2\pi}{\lambda_z}$ in Equation 7 results in the Linearized Navier-Stokes (LNS) equation,

$$\left(\frac{\bar{A}}{h_1}-\frac{i\beta\bar{V}_{xz}}{h_3Re_0}\right)\frac{\partial\chi}{\partial x}+\left(\bar{B}+\frac{i\beta\bar{V}_{yz}}{h_3Re_0}\right)\frac{\partial\chi}{\partial y}+\left(\bar{D}-i\omega\bar{\Gamma}+\frac{i\beta\bar{C}}{h_3}+\frac{\beta^2\bar{V}_{zz}}{h_3^2Re_0}\right)\chi = \frac{1}{Re_0}\left(\frac{\bar{V}_{xx}}{h_1^2}\frac{\partial^2\chi}{\partial x^2}+\frac{\bar{V}_{xy}}{h_1}\frac{\partial^2\chi}{\partial x\partial y}+\bar{V}_{yy}\frac{\partial^2\chi}{\partial y^2}\right). \tag{9}$$

This equation can be solved as an eigenvalue problem, and simplifications lead to approximate solutions that are obtained at a lower computational cost for engineering applications. One such simplification is the quasiparallel assumption that neglects velocity normal to the wall and all mean flow variation in the x direction. The quasiparallel assumption leads to the Linear Stability Theory (LST) solutions. The linear Parabolized Stability Equations (PSE) decompose the mode shape into two parts: a complex wave number α that varies only in x and a shape function that varies in x and y,

$$\chi = \chi(\hat{x}, y)e^{i\int_{x_0}^{x}\alpha(\xi)d\xi}. \tag{10}$$

Equation Set 1 applies to a calorically perfect gas. The results included in this work use either a mixture of thermally perfect gases using a finite-rate chemical kinetic model, and thermochemical nonequilibrium. In order to address these models, the equations are rederived to include updated relationships for transport and thermodynamic properties. The resulting equations remain in the same form shown in Equation 9, with the contents and dimensions of ϕ, χ, and the Jacobian matrices updated.

For finite-rate chemistry, additional equations are necessary to calculate the species mass fractions and their disturbances. The continuity and momentum equations remain unchanged, using mixture values for ρ, p, and μ. Equations governing species production and destruction are added, and the energy equation must be updated to include energy changes from the chemical reactions. Drawing from MacCormack and Candler [34], Chang et al. [18] and Anderson [35], and nondimensionalizing,

$$\begin{aligned}
\rho\left(\frac{\partial C_s}{\partial t}+\nabla\cdot\left(C_s\vec{V}\right)\right) &= \frac{Le}{RePr}\nabla\cdot(\rho D_s\nabla C_s)+\dot{\omega}_s,\ \ s=1\ldots N_s \\
\rho C_p\left[\frac{\partial T}{\partial t}+(\vec{V}\cdot\nabla)T\right] &= \frac{1}{RePr}\nabla\cdot(k\nabla T)+Ec\left(\frac{\partial p}{\partial t}+(\vec{V}\cdot\nabla)p\right)+Ec\frac{\Phi}{Re} \\
&\quad+\frac{Le}{RePr}\sum_{s=1}^{N_s}\left(\nabla(h_s)\cdot(\rho D_s\nabla C_s)\right)+\sum_{s=1}^{N_s}h_s\dot{\omega}_s,
\end{aligned} \tag{11}$$

where:

$$\begin{aligned}
C_p &= \sum_{s=1}^{N_s}C_sC_{p,s} \\
\rho &= \sum_{s=1}^{N_s}\rho_s = \frac{p}{R_u\sum\frac{C_s}{M_s}T} \\
C_s &= \rho_s/\rho\ ,\ \sum C_s = 1 \\
\dot{\omega}_{s,d} &= M_s\sum_{r=1}^{N_r}\left(\beta_{s,r}-\alpha_{s,r}\right)\left(R_{f,r}-R_{b,r}\right) \\
\dot{\omega}_s &= \dot{\omega}_{s,d}\frac{\ell}{\rho_e u_e}\ .
\end{aligned} \tag{12}$$

M_s is the species molecular mass, R_u the universal gas constant, ρ_s is the species density, N_s is the number of species in the gas mixture, $\dot{\omega}_s$ represents the nondimensionalized species production rate due to chemical reactions, D_s is the diffusivity of species s with respect to the gas mixture normalized by the value at the boundary-layer edge D_e, and h_s is the enthalpy per unit mass of species s nondimensionalized by edge temperature and heat capacity. The terms $\beta_{s,r}$ and $\alpha_{s,r}$ are the stoichiometric coefficients for the N_r reactions being considered, and $R_{f,r}$ and $R_{b,r}$ are the associated reaction rates. Equation Set 11 is nondimensionalized in a manner similar to Equation Set 1. The mean

flow disturbance vector now includes species mass fractions, $C_s = \bar{C}_s + C'_s$, in addition to the disturbances listed in Equation 5. The governing equation for the disturbances including species mass fractions can be expressed in the same form as Equation 6, with the difference that the Jacobians are now of a larger dimension and contain terms from the species mass fraction equations and new terms in the energy equation that depend on the mass fractions.

In the previous equations, thermal equilibrium was assumed. This means that the vibrational, electron, translational, and rotational energies had equilibrated and a single temperature is sufficient. *In other words, we assume that the relaxation time between these energy modes is sufficiently shorter than the time scale of the flow phenomena. This is not necessarily true for hypersonic problems.* For thermal nonequilibrium, multiple temperatures are required. In this work, we will use a two-temperature model for thermochemical equilibrium, where the vibrational-electronic energies are associated with $T_V = T_{vib} = T_{el}$, and the translational-rotational energy is associated with $T = T_{trans} = T_{rot}$. As compared to thermal equilibrium with chemical nonequilibrium (the finite-rate chemistry model), an additional equation and variable are added to the system, with the associated disturbance T'_V. In addition, the chemistry model will take into account different rate controlling temperatures based on T and T_V depending on what type of reaction is occurring. The total energy equation is updated,

$$\begin{aligned}\rho C_p \left[\frac{\partial T}{\partial t} + (\vec{V}\cdot\nabla)T\right] + \rho C_{p,V}\left[\frac{\partial T_V}{\partial t} + (\vec{V}\cdot\nabla)T_V\right] &= \frac{1}{RePr}\nabla\cdot(k\nabla T + k_v\nabla T_V) + Ec\left(\frac{\partial p}{\partial t} + (\vec{V}\cdot\nabla)p\right)\\ &+ Ec\frac{\Phi}{Re} + \frac{Le}{RePr}\sum_{s=1}^{N_s}\Big(\nabla(h_s)\cdot(\rho D_s\nabla C_s)\Big) + \sum_{s=1}^{N_s} h_s\dot{\omega}_s\,,\end{aligned} \tag{13}$$

and a vibrational-electronic energy equation is added:

$$\begin{aligned}\rho C_{p,V}\left[\frac{\partial T_V}{\partial t} + (\vec{V}\cdot\nabla)T_V\right] &= \frac{1}{RePr}\nabla\cdot(k_v\nabla T_V) + Ec\left(\frac{\partial p_{el}}{\partial t} + (\vec{V}\cdot\nabla)p_{el}\right)\\ &+ \frac{Le}{RePr}\sum_{s=1}^{N_s}\Big(\nabla(h_{v,s})\cdot(\rho D_s\nabla C_s)\Big)\\ &+ \sum_{s=mol}\rho_s\frac{(e^*_{v,s} - e_{v,s})}{<\tau_s>} + 2\rho_{el}\frac{3}{2}\bar{R}(T - T_V)\sum_{s=1}^{N_s-1}\frac{\nu_{es}}{M_s} - \sum_{s=ions}\dot{n}_{e,s}\hat{I}_s + \sum_{s=1}^{N_s}\dot{\omega}_s\hat{D}_s\,,\end{aligned} \tag{14}$$

where the T_V is normalized by the boundary layer edge value of the translational temperature T_e, $C_{p,V}$ is the constant pressure specific heat for electron-vibrational energy modes and $\int_0^{T_V} C_{p,V}\,dT = e_v$, the combined electron and vibrational energy. $C_{p,V}$ is normalized by the edge specific heat $C_{p,e}$, and the remaining terms are similarly nondimensionalized. The vibrational thermal conductivity k_v, vibrational-translational relaxation time $<\tau_s>$, species vibrational enthalpy $h_{v,s}$, vibrational energy per unit mass of diatomic molecules $\hat{D}_s$ have been added, and are provided by the chemistry model. In this work, electron and ion species are not included, and so ionization and electron related terms such as the electron pressure p_{el}, collision frequency between electrons and neutral particles ν_{es}, rate of ion production $\dot{n}_{e,s}$ and ionization energy $\hat{I}_s$ will not be needed. Terms dependent on the chemistry model are discussed further in Section B, and terms specific to thermochemical nonequilibrium in Equations 23–27.

The included results are presented in terms of a nondimensional frequency F, the complex part of the wavenumber α_i, and the N-factor based on disturbance kinetic energy,

$$\begin{aligned} F &= \frac{2\pi\ell}{u_e}f\\ \alpha_i &= \Im\left(\alpha(x)\right)\\ E &= \int_0^{y_e}\rho(|u'|^2 + |v'|^2 + |w'|^2)dy\\ \sigma(x) &= -\alpha_i(x) + \frac{1}{2E}\frac{dE}{dx}\\ N(x) &= \int_{x_0}^{x}\sigma(\xi)d\xi = \log\left(\frac{A}{A_0}\right).\end{aligned} \tag{15}$$

The N-factor N refers to the logarithm of the amplitude change of a disturbance with initial amplitude A_0, calculated using the integrated growth rate, σ, based on disturbance kinetic energy E, which is evaluated to the edge of the

boundary layer y_e. The integral defining N is evaluated with the neutral point where the imaginary growth rate first becomes negative as the lower bound. The critical N-factor (N_{crit}) is the value of the N-factor where transition would be expected to occur based on experimental correlations. When α_i is negative the associated eigenmode is unstable.

B. Chemical Rates and Thermodynamic Properties

A number of the quantities needed for boundary layer stability are dependent on the gas composition, including species production rates $\dot{\omega}_s$, transport properties viscosity and thermal conductivity, and thermodynamic quantities of specific heats and enthalpy. The chemistry model used in this work is similar to that developed by Thompson et al.[36] for the calculation of thermodynamic and transport properties, with modifications to the curve fits used and additional data introduced to accommodate Martian atmospheric composition. The chemistry model used in this work uses the Chemical Equilibrium with Applications (CEA) format for thermodynamic curve fit coefficients, with the equations for specific heat, enthalpy, and entropy for each species from McBride et al.[37]:

$$\begin{aligned} C_{p,s}(T)/R &= a_1T^{-2} + a_2T^{-1} + a_3 + a_4T + a_5T^2 + a_6T^3 + a_7T^4 \\ h_s(T)/RT &= -a_1T^{-2} + a_2\ln T/T + a_3 + a_4T/2 + a_5T^2/3 + a_6T^3/4 + a_7T^4/5 + b_1/T \\ S_s(T)/R &= -a_1T^{-2}/2 - a_2T^{-1} + a_3\ln T + a_4T + a_5T^2/2 + a_6T^3/3 + a_7T^4/4 + b_2\,, \end{aligned} \tag{16}$$

where the equations for enthalpy and entropy use the same coefficients as the equation for specific heat and are found by integrating $C_{p,s}$ and $C_{p,s}/T$ with respect to T. The Gibbs free energy can then be determined from the enthalpy and entropy for use in calculating the equilibrium state through minimization of the free energy. The constants for this curve fit are available from [38].

In addition to the thermodynamic quantities, transport quantities of viscosity, thermal conductivity, and diffusion coefficients are required. These quantities are calculated as functions of collision integrals between all pairs of chemical species included in the model. The collision integrals or collision cross-sections $\pi\bar{\Omega}_{i,j}^{(l,s)}$ for momentum transfer are defined as integrated functions of the differential cross section for the pair of species, the relative velocity and reduced velocities of the colliding particles, and the scattering angle. This equation can be found in Yos[39], and rather than evaluate the detailed expression for the collision cross-section at each temperature, curve fits based on cross-section values evaluated at a range of temperatures are used commonly in literature [40, 41]. A curve fit for air is available from Gupta et al.[40].

The curve fits for collision integrals between species of air are given in Thompson et al.[36] in the following form:

$$\begin{aligned} \pi\bar{\Omega}_{ij}^{(1,1)} &= \exp(D_{ij}^{(1,1)})T^{[A_{ij}^{(1,1)}\ln T^2 + B_{ij}^{(1,1)}\ln T + C_{ij}^{(1,1)}]} \\ \pi\bar{\Omega}_{ij}^{(2,2)} &= \exp(D_{ij}^{(2,2)})T^{[A_{ij}^{(2,2)}\ln T^2 + B_{ij}^{(2,2)}\ln T + C_{ij}^{(2,2)}]}\,. \end{aligned} \tag{17}$$

Modified collision integrals are required for transport properties,

$$\begin{aligned} \Delta_{ij}^{(1)}(T) &= \frac{8}{3}\left[\frac{2M_iM_j}{\pi R_uT(M_i+M_j)}\right]^{1/2}\pi\bar{\Omega}_{ij}^{(1,1)} \\ \Delta_{ij}^{(2)}(T) &= \frac{16}{5}\left[\frac{2M_iM_j}{\pi R_uT(M_i+M_j)}\right]^{1/2}\pi\bar{\Omega}_{ij}^{(2,2)}, \end{aligned} \tag{18}$$

where R_u is the universal gas constant and M_i is the molecular mass of species i.

Coefficients for curve fits for a Martian atmosphere were calculated using tabulated values from Wright et al.[42], using minimization of the mean square difference with the tabulated values. Viscosities calculated using this curve fit compared well with polynomial curve fits for viscosity provided by Chemical Equilibrium with Applications [38]. According to collision integral data tabulated in by Wright[42], the uncertainty in the values of the collision integrals ranges anywhere from ±5% to ±50%, and so although a curve fit can match the data closely, it should not be expected to be any more accurate than the data used.

The temperature used in these equations varies depending on the participants in the collision if a multitemperature model is used. For example, collisions involving electrons should use the electron temperature in a three-temperature model, or the vibration-electron temperature in a two-temperature model. The viscosity (μ), translational thermal conductivity (k), and molecular diffusion coefficients (D_i) are expressed as approximate functions of the modified

collision integrals,

$$\begin{aligned}
\mu &= \sum_{i}^{N_s} \frac{m_i \gamma_i}{\sum_{j}^{N_s} \gamma_j \Delta_{ij}^{(2)}(T)} \\
k &= \frac{15}{4} k_B \sum_{i}^{N_s} \frac{\gamma_i}{\sum_{j \neq e}^{N_s} \alpha_{ij} \gamma_j \Delta_{ij}^{(2)}(T) + 3.54 \gamma_e \Delta_{ie}^{(2)}(T_{el})} \\
D_{ij} &= \frac{k_b T}{p \Delta_{ij}^{(1)}(T)} \\
D_i &= \frac{(\sum_k \gamma_k) M_i (1 - M_i \gamma_i)}{\sum_{j \neq i} (\gamma_j / D_{ij})},
\end{aligned} \tag{19}$$

where in a two-temperature model as used in this work $T_{el} = T_v = T_V$, and the subscript el indicates the electron species. For a one-temperature model $T_{el} = T_v = T_{tr} = T$. The coefficient α_{ij}, not to be confused with the imaginary component of the complex wave number, is defined as:

$$\alpha_{ij} = 1 + \frac{(1 - (m_i/m_j))(0.45 - 2.54(m_i/m_j))}{(1 + (m_i/m_j))^2}, \tag{20}$$

and m_i is the particle mass, or the molecular mass divided by Avogadro's number and $\gamma_i = \frac{\rho_i}{\rho M_i}$ is the molar concentration. D_i is the molecular diffusion coefficient of species i with respect to the gas mixture, whereas D_{ij} is the diffusion coefficient of species i with respect to species j or vice versa. For a multitemperature model, rotational/vibrational and/or electron thermal conductivity would also be required, and the electron temperature should be used for each term in the summation involving an electron collision. In a two-temperature model as used in this work, the electron temperature is equal to the vibrational temperature.

The species production rate $\dot{\omega}_s$ is a function of chemical reaction rates ($R_{f,r}(T)$, $R_{b,r}(T)$) and the stoichiometric coefficients ($\alpha_{i,r}$, $\beta_{i,r}$) for the relevant chemical reactions included in the model with species s, reaction r,

$$\begin{aligned}
\sum_{s}^{N_s} X_s \alpha_{s,r} &\rightleftharpoons \sum_{s}^{N_s} X_s \beta_{s,r} \\
\dot{\omega}_s &= M_i \sum_{r=1}^{N_r} (\beta_{s,r} - \alpha_{s,r}) \left(R_{f,r} - R_{b,r} \right) \\
R_{f,r} &= 10^3 \left[k_{f,r}(T) \prod_{s=1}^{N_s} \left(\frac{10^{-3} C_s \rho}{M_s} \right)^{\alpha_{s,r}} \prod_{k=N_s+1}^{N_J} \left(10^{-3} \sum_{s=1}^{N_s} Z_{k,s} \frac{C_s \rho}{M_s} \right)^{\alpha_{k,r}} \right],
\end{aligned} \tag{21}$$

where scaling factors are used to account for terms traditionally expressed in cm and g, and ρ is the mixture density. N_s is the number of species and N_J is the total number of reactants including catalytic third bodies accounted for using the third body efficiencies $Z_{k,s}$. The rate constant $k_{f,r}$ is expressed in the modified Arrhenius form, with coefficients based on empirical results:

$$k_{f,r}(T_c) = A T_c^B \exp(T_d / T_c), \tag{22}$$

where A, B, and T_d are the modified Arrhenius coefficients. T_d is the ratio of the activation energy and the gas constant, E_a/R. T_c is the rate-controlling temperature, and is a function of the vibrational and translational temperatures. In single-temperature models, $T_c = T = T_V$. In multitemperature models, the rate-controlling temperature is determined by the type of reaction, where $T_c = \sqrt{T T_V}$ as used by Park [26, 43] for dissociation reactions and $T_c = T$ for heavy molecule collision reactions. A similar form is used for the backwards reaction rate $R_{b,r}$ either using backwards rate Arrhenius coefficients with the Dunn & Kang model or with a rate constant determined using the equilibrium constant; $k_{b,r} = k_{f,r}/K_{eq}$ with K_{eq} computed through minimization of Gibbs free energy.

In this work, the coefficients for Equation 22 are drawn from Park [26] for the Martian atmosphere model and from the Dunn & Kang model[44] as reviewed by Gupta et al.[40] for the air gas model. Noncatalytic boundary conditions are used at the surface in both mean flow and disturbance equations. Although ionization and radiation effects are expected to be significant for reentry applications, these effects are neglected in the current work due to the increased

complexity and computational cost. These effects may be included in the future. Effects of ablation and chemical reactions with ablation products are also neglected. Results presented in this work include one- and two- temperature models. Ionization, ablation, and three-temperature models are outside the scope of this work, where the next reasonable step to increase complexity and accuracy would be the addition of ionization effects. Although more modern chemical models are available, these well established chemical models allow comparison to results in the literature without introducing differences due to reaction rates, and Armenise et al. [21] found that the multitemperature approach by Park et al. [26] compares well with the higher-fidelity state-to-state method. The modifications to LASTRAC have been implemented such that it will be straightforward to replace this model with an arbitrary user-defined chemical model in the future.

A number of additional terms are required for thermochemical nonequilibrium flow. As the gas mixture used in this work contains only neutral atomic and diatomic species, terms such as the the electron pressure p_{el}, collision frequency between electrons and neutral particles ν_{es}, rate of ion production $\dot{n}_{e,s}$ and ionization energy $\hat{I}_s$ will not be discussed in detail. These terms can be found in reference [41].

Continuing to follow Gnoffo [41], for a two-temperature model, the vibrational-electronic heat capacity for diatomic molecules is calculated as:

$$C^s_{v,V}(T_V) = C^s_v(T_V) - \frac{5}{2}\frac{R_u}{M_s}, \tag{23}$$

where $C^s_{v,V}$ is the vibrational-electronic heat capacity for species s, $C^s_v(T_V)$ is the heat capacity for species s produced from curve fits for $C_v = C_p - \frac{R_u}{M_s}$ at the vibrational-electronic temperature T_V, and the final term is the subtraction of the heat capacity of the translational and rotational energy modes. The heat capacity for the translational-rotational modes is:

$$\begin{aligned} C^s_{p,tr} &= C^s_{v,rot} + C^s_{v,trans} + \frac{R_u}{M_s} = \frac{R_u}{M_s} + \frac{3}{2}\frac{R_u}{M_s} + \frac{R_u}{M_s} = \frac{7}{2}\frac{R_u}{M_s} \\ C^s_{v,tr} &= C^s_{v,rot} + C^s_{v,trans} = \frac{5}{2}\frac{R_u}{M_s}, \end{aligned} \tag{24}$$

where these equations are independent of temperature because the translational and rotational energy modes are assumed to be fully excited. In these equations the molecules are assumed to be linear molecules, where nonlinear molecules would have an additional rotational degree of freedom. At very low temperatures, the difference between homonuclear (O_2, N_2) and heteronuclear (NO) molecules would also need to be considered, however, we assume fully excited rotational modes in this work. This model will need to be updated in the future to account for nonlinear polyatomic molecules, and greater accuracy especially at high and low temperatures, where traditional curve fits are less accurate, may be possible through explicitly evaluating the vibrational partition function. For monoatomic species other than the electron species, $C^s_{v,V} = 0$ and the curve fit for specific heat is used directly. Similarly, the vibrational-electronic enthalpy per species $h_{v,s}$ is only nonzero for molecules. For these molecules, the translational-rotational enthalpy is also adjusted,

$$\begin{aligned} h_{tr,s} &= h_s(T) + C_{p,s}(T - T_V) \\ h_{v,s} &= h_s(T_V) - C_{p,s}(T_V - T_{ref}) + h_{ref}, \end{aligned} \tag{25}$$

where $h_s(T)$ is the evaluation of the curve fit for enthalpy used for the single-equation model shown in Equation Set 16, with T_{ref} and h_{ref} being the reference conditions of those curve fits. These equations are similar to those found in [41], using curve fits in the CEA format [38].

The term involving $(e^*_{v,s} - e_{v,s}) \approx \left(C^s_{v,V}(T)T - C^s_{v,V}(T_V)T_V\right)$ represents the relaxation between vibrational-electronic and translational-rotational energy modes, where $e^*_{v,s}$ is the vibrational-electronic energy evaluated at the translational temperature T, and $e_{v,s}$ is the vibrational-electronic energy evaluated at the vibrational-electronic temperature T_V. The vibrational-translational energy relaxation time for diatomic molecules is found using the

Millikan-White correlation [45] and a collision cross-section correction by Park [46]:

$$
\begin{aligned}
< \tau_s > &= \tau_s^{MW} + \begin{cases} \tau_s^P & T > 8000\,K \\ 0 & T < 8000\,K \end{cases} \\
\tau_s^{MW} &= \frac{1}{p_{atm}} \frac{\sum_{i=1,\neq e^-}^{N_s} n_i e^{A_s\left(T^{1/3}-0.015\mu_{si}^{1/4}\right)-18.42}}{\sum_{i=1,\neq e^-}^{N_s} n_i} \\
\tau_s^P &= (\sigma_s \bar{c}_s n_s)^{-1} \\
\bar{c}_s &= \sqrt{(8k_B T/\pi(M_s/Av))},
\end{aligned}
\tag{26}
$$

where τ_s^{MW} is the Millikan and White [45] semi-empirical correlation, and τ_s^P is the Park [46] correction, using $\sigma_s = 10^{-16}\,cm^2$ as used by Gnoffo [41], Av is Avogadro's number such that M_s/Av is the mass per particle of species s in kg, and $n_s = C_s/M_s$ is the number density per species. Unlike [41], we use τ_s directly rather than an averaged term. For thermochemical nonequilibrium flow, the state equation should also be updated in the presence of electrons:

$$
p = \sum_{s=1,s\neq e^-}^{N_s} \left(\rho_s \frac{R_u}{M_s} T\right) + \rho_{el} \frac{R_u}{M_{el}} T_V\,, \tag{27}
$$

where in this work electron species are not included, and this reduces to the previously-used state equation. The final term of Equation 14 represents the production of vibrational energy due to the creation and destruction of diatomic molecules with the vibrational energy per unit mass of the molecules represented by $\hat{D}_s$. The approximation suggested by Park [47], $\hat{D}_s = \tilde{D}_s - k_B T$, is used with the dissociation energy $\tilde{D}_s$ taken from tabulated values. This makes the assumptions that there is preferential dissociation and recombination of the molecules in the higher vibrational states, and that the vibrational energy removed by dissociation differs by the average translational energy.

C. Mean Flow Solutions

Two legacy boundary layer codes were used to generate the mean flow solutions for the simple geometries used for verification. Blottner's chemical nonequilibrium boundary layer code [48] and the BOLAY 11 [49] code are both Fortran codes capable of generating similarity-based flow solutions for simple geometries. The former is capable of generating boundary layers with finite-rate chemistry, while the latter can generate boundary layers with either calorically perfect gas or chemical equilibrium. Small modifications to these codes were required to output in the LASTRAC input format, and for compatibility with modern Fortran compilers. Mean flow solutions for results comparing between the two atmospheres use VULCAN[50, 51] with a Martian atmosphere model and an air model that use the same species compositions and Arrhenius coefficients as described in Section B. Both finite-rate chemistry and thermochemical nonequilibrium with a two-temperature model were used to generate VULCAN solutions. In order to more closely match boundary layer solution results and eliminate leading edge effects as much as possible, the CFD mesh begins at the leading edge, with freestream conditions imposed immediately ahead of the flat plate. CFD solutions were converged to a residual reduction of at least 4 orders of magnitude. Grid dimensions were 993x497 points with approximately 200-300 points clustered in the boundary layer, and points clustered towards the leading edge. A finer grid with doubled dimensions of 1985x993 was also tested. Comparison of stability results between the finer and coarser grids were closely aligned, and so the coarser grid was used for the majority of simulations. CFD meshes were generated using Pointwise®. Past investigations using LASTRAC have indicated that around 100 points inside the boundary layer give accurate stability results. High grid counts are used here to ensure grid-converged solutions and may not be necessary.

Despite attempts to ensure that the CFD simulation was as close as possible to boundary layer similarity solutions, a weak shock was encountered in the flow solution that slightly modified the edge conditions of the boundary layer. This shock forms due to the growth of the boundary layer at the leading edge, which displaces the streamlines close to the wall. Although this shock is weak, and grows weaker with distance from the leading edge, it is strong enough to have a slight effect on the stability results within the 1 meter length of the flat plate used in the results.

IV. Results

This section first reproduces a selected verification result for a Mach 10 adiabatic flat plate in air. Further verification results in air for the same capabilities can be found in related work[19]. Verification of PSE for Martian atmosphere was

not conducted due to a lack of similar results to compare against. Section B compares results using a $CO_2 - N_2$ Martian atmosphere model under the same nondimensional conditions, including PSE computations of supersonic modes under the Martian atmosphere.

A. Verification

Verification of LASTRAC with newly-implemented support for equilibrium and finite-rate chemistry was presented by Kline et al. [19]. Here we repeat one of the verification cases, a Mach 10 adiabatic flat plate. The flat plate case will then be repeated with the Martian atmosphere chemistry to investigate the effect of changing gas composition on the stability of the boundary layer. The case of Mach 10 flow over an adiabatic flat plate with a boundary layer edge temperature of 350 K, edge velocity of 3751 m/s, and edge pressure of 3.55 kPa has been investigated repeatedly in literature [18, 52–54] under assumptions of perfect, equilibrium, and finite-rate chemistry. Results in literature provide both a number of options to compare against as well as providing an idea of the expected discrepancy between solutions that would be considered reasonable. Using Sutherland's law for viscosity and the stated edge conditions from literature produce $Re_u \approx 6.5 \times 10^6/m$. In this work, the static edge conditions are matched, resulting in $Re_u \approx 6.5 \times 10^6/m$ where the inclusion of chemical and thermal effects results in different viscosity and density values. An adiabatic and noncatalytic wall boundary condition is used.

The comparison between growth rates for for gas models over a range of frequencies can be seen in Figure 1. This figure includes selected results from the literature [18, 54, 55]. Results from the literature are plotted using digitized scanned images from published results, which were then smoothed using Tecplot® data smoothing tools. From this plot, we can conclude that the current implementation is matching previously published results within the variability seen between different sources. Values are plotted at a local Reynolds number based on length scale ($\sqrt{Re_x} = u_e \ell / \nu_e$) of 2000, where the length scale is defined as $\ell = \sqrt{\nu_e x / u_e}$.

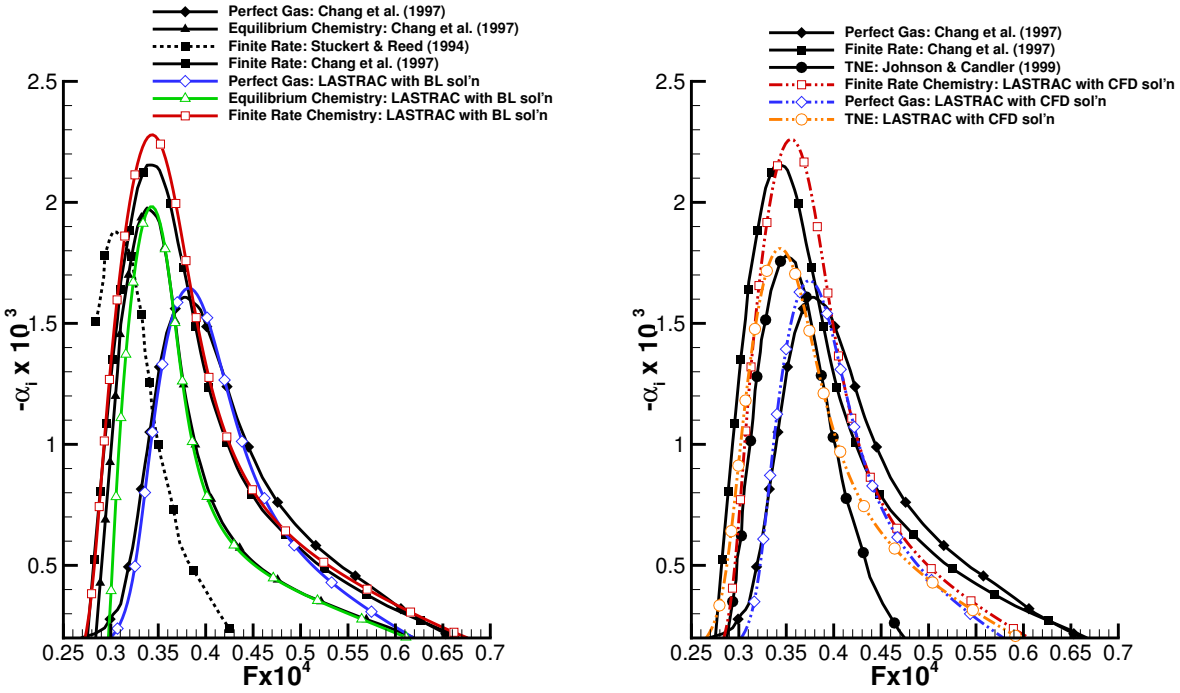

(a) Comparison using boundary layer codes at $\sqrt{Re_x}$=2000.

(b) Comparison using VULCAN CFD results at $\sqrt{Re_x}$=2000.

Fig. 1 Mach 10 adiabatic flat plate disturbance growth rates compared against Chang et al. [18], Stuckert & Reed [54], and Johnson et al. [55].

Further verification cases of a two-dimensional wedge and an axisymmetric cone in air are included in related work[19].

B. Comparison of Earth and Mars Boundary Layer Stability at Nondimensionally Similar Conditions

In this section the effects of switching from five-species air to eight-species Martian atmosphere gas chemistry are examined through variations on the Mach-10 flat plate. VULCAN[50, 51] was used to generate finite-rate and thermochemical nonequilibrium flow solutions for both air and Martian atmospheres. Flow conditions are Mach 10, freestream unit Reynolds number $Re_u \approx 6.5 \times 10^6$ per meter, and freestream static temperature 350 K. This corresponds to the flat plate case used in Figure 1, with conditions of the Mars atmosphere case set to share the nondimensional parameters M and Re_u and the same freestream temperature. Although not an accurate reflection of Martian atmospheric entry conditions, this provides an example with nonequilibrium effects, and attempts to isolate the effect of changing the gas composition.

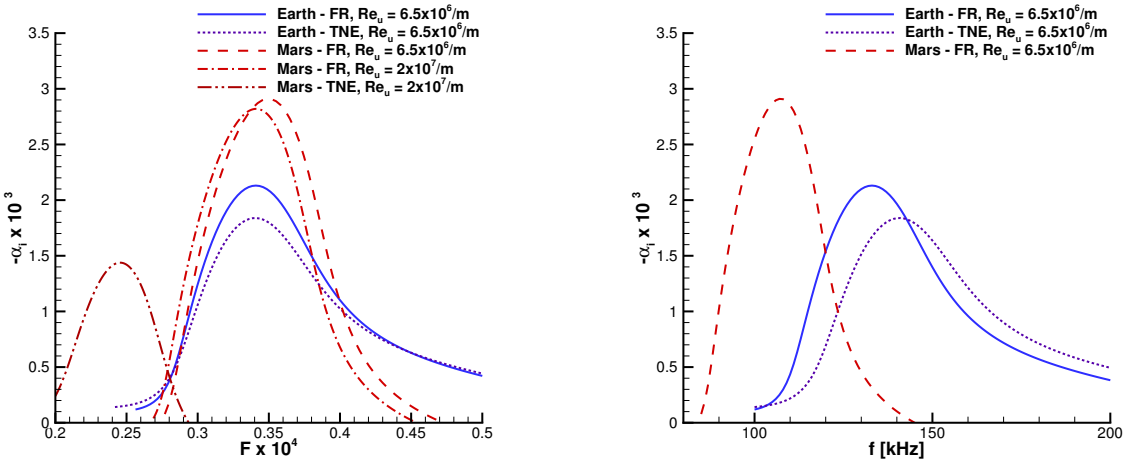

(a) Nondimensionalized frequency as defined in Equation 15.

(b) Dimensional frequency, with freestream $Re_u = 6.5 \times 10^6/m$.

Fig. 2 Disturbance growth rates for a Mach 10 adiabatic flat plate at $\sqrt{Re_x}$=2000 with finite-rate or thermochemical nonequilibrium assumptions, with two gas compositions.

From Figure 2, we can see that at a constant Reynolds number the effect of changing from air (O_2-N_2) to a Martian atmosphere (CO_2-N_2) has a destabilizing effect on the most-amplified peak with finite-rate chemistry, and stabilizing with thermochemical nonequilibrium. From Figure 2a we can see that the nondimensionalized peak frequency has shifted only slightly, while the dimensional peak frequency for the Martian atmosphere is shifted further. The case of thermochemical nonequilibrium at freestream unit Reynolds number of 6.5×10^6 per meter was not able to find an unstable solution, however, results at a higher freestream unit Reynolds number are included in this plot to illustrate the stabilizing effect of thermochemical nonequilibrium on the Martian atmosphere case. This alternate case is also included in later plots where noted.

Figure 3 plots the N-factor versus the nondimensional term for the distance, $\sqrt{Re_x}$, at a selection of frequencies, for both Air and Martian atmosphere with finite-rate chemistry in Figure 3a. Figure 3b illustrates the same scenario with thermochemical nonequilibrium, where due to LASTRAC not finding unstable modes for the same unit Reynolds number, the higher unit Reynolds number case is used. Figure 3b uses a different range of nondimensional frequencies due to the shifted unstable frequency range shown in Figure 2. Under finite rate chemistry assumptions, the Martian atmosphere case is more unstable, and would be predicted to transition earlier than in air. However, when thermochemical nonequilibrium effects are included it is clear that the Martian boundary layer is more stable, and would transition at a later point. The overall N-factors appear to be small for the flat plate configuration investigated. At larger Reynolds number or higher temperature during reentry, more instability and higher N-factors should be expected, although the trends in comparing between the different gas models should be similar.

Plotting the N-factor versus distance such as in Figure 3 gives an estimate of where along the plate transition is likely to occur, often taken as the point where the N-factor exceeds a critical value. The specific critical N-factor depends on the conditions of the flight or wind tunnel test, and must be experimentally determined. Since the overall N-factor in these plots is much lower than usual critical values closer to ≈ 8, a small N-factor of 1.5 is highlighted to illustrate the

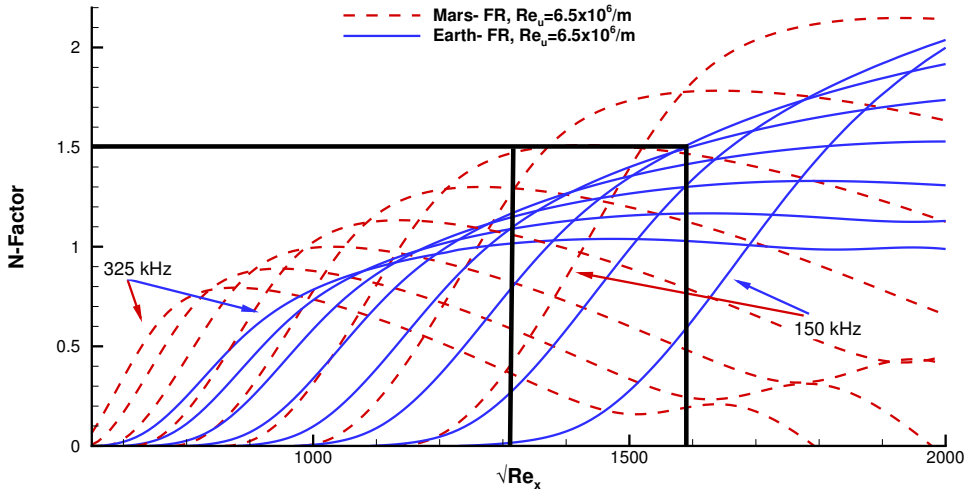

(a) Finite-Rate Chemistry, at freestream $Re_u = 6.5 \times 10^6/m$.

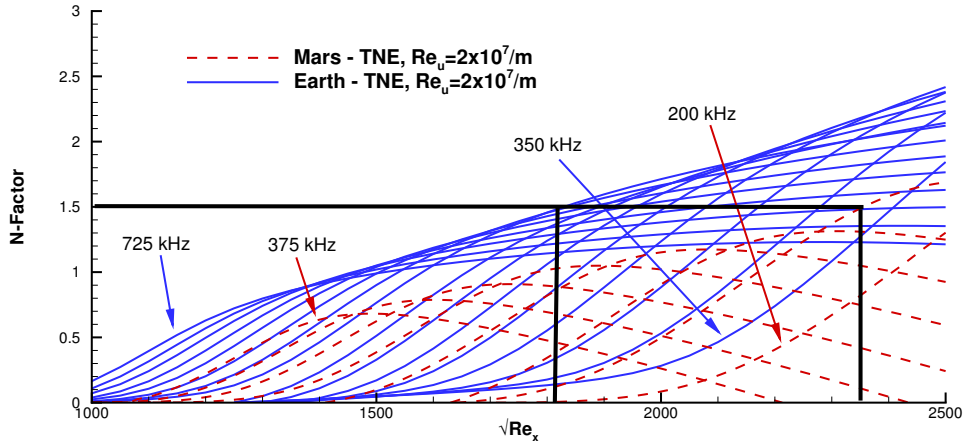

(b) Thermochemical nonequilibrium, at freestream $Re_u = 2 \times 10^7/m$.

Fig. 3 N-factor versus $\sqrt{Re_x}$ for a Mach 10 flat plate using LST. Labels indicate the disturbance frequency, with unlabeled lines in increments of 25 kHz. Thick black lines illustrate an estimate of the change in transition Reynolds at a low critical N-Factor.

an estimated change in transition Reynolds number. Under assumptions of finite-rate chemistry the boundary layer reaches this value at a lower $\sqrt{Re_x}$, while with thermochemical nonequilibrium effects taken into account transition would be expected at a later $\sqrt{Re_x}$.

Figure 4 illustrates the results of evaluating PSE using thermochemical nonequilibrium gas in a Martian atmosphere mixture at a selection of disturbance frequencies, compared against LST results at the same frequencies. These results show the 2nd Mack mode, and in the PSE a supersonic mode is also encountered. The oscillations in the N-factor plot are often seen in the neighborhood of supersonic modes, and the phase speed plot in Figure 4b confirms the presence of supersonic modes by showing that the phase speed dips below the limiting value of $1 - 1/M_e$. The supersonic mode is associated with acoustic-wave like radiation of disturbances outside the boundary layer region, and in order to capture this mode accurately nonreflecting boundary conditions should be used at the freestream boundary of the PSE analysis, as was done in this case. The supersonic mode increases the N-factor and delays the decay of the N-factor downstream of the 2nd mode. The increase in N-factor of 1-2 in Figure 4a indicates that there is a strong nonparallel effect due to

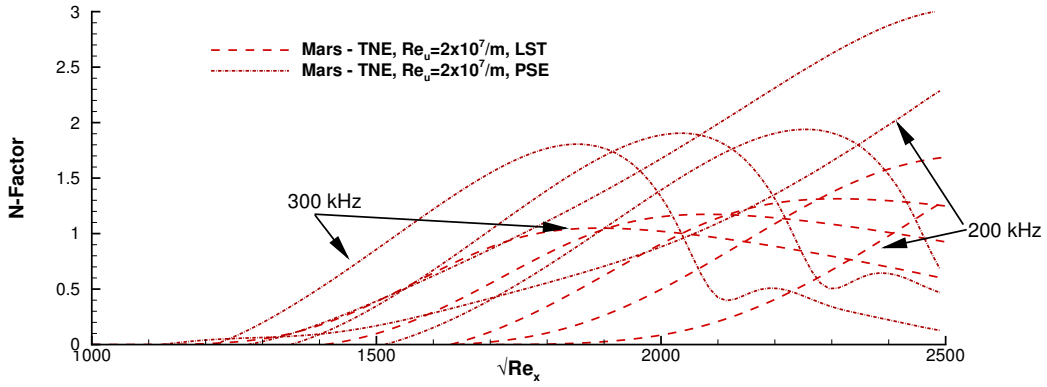

(a) N-factor versus nondimensional streamwise distance for a selection of frequencies comparing PSE against LST.

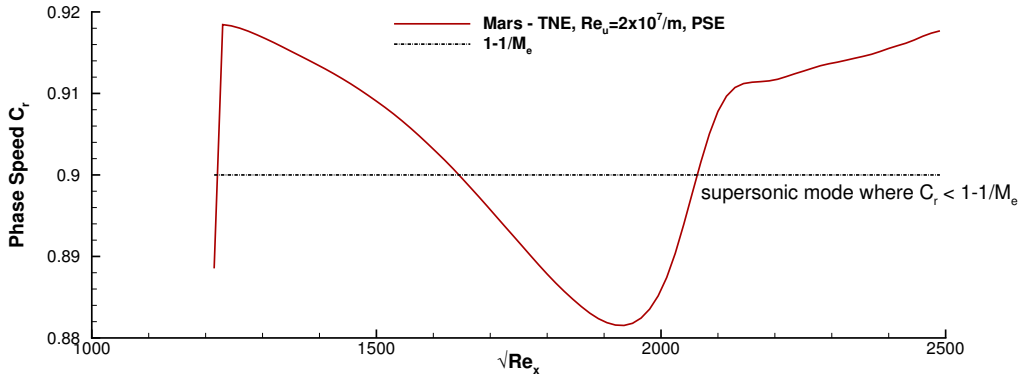

(b) Phase Speed versus nondimensional streamwise distance at a disturbance frequency of 300 kHz.

Fig. 4 PSE and LST results with CO_2-N_2 mixture and thermochemical nonequilibrium gas at freestream $Re_u = 2 \times 10^7/m$.

boundary layer growth. Since the N-factor is a logarithmic quantity as defined in Equation 15, this translates to 1-2 orders of magnitude increase in the growth of the disturbance magnitude.

The differences between the Martian and Earth stability results may be greater under higher-temperature conditions, such as those encountered under atmospheric entry, due to the greater degree of nonequilibrium phenomena.

V. Conclusions

The tools implemented in this work allow analysis of the boundary layer stability in a Martian atmosphere, building on the capability to address both chemical and thermochemical nonequilibrium implemented in previous work[19]. In this work, these tools were applied to comparisons of boundary layer stability for Martian atmosphere modeled as an 8-species mixture with 97% CO_2 and 3% N_2 and under air modeled as a 5-species mixture of 21% O_2 and 79% N_2, using nondimensionally similar freestream conditions and a simple flat plate geometry. Transport properties in the reacting Martian atmosphere were calculated using curve fits to collision integral data available in literature. The Mach 10 adiabatic flat-plate case considered has been studied thoroughly in air, and this work compares the same case in Martian atmosphere, with a higher-Reynolds number variation included due to the absence of unstable modes at the baseline conditions for thermochemical nonequilibrium in the Martian atmosphere model. Ablation, radiation, and ionization, although relevant to Martian atmospheric entry, have been neglected in this work due to the increased complexity and computational cost, and may be included in the future. The flat plate is adiabatic with a noncatalytic assumption applied at the wall.

The included results illustrate the differences between boundary layer stability results in terms of N-factors and growth rates. Figure 2 showed that the inclusion of thermochemical nonequilibrium has more significant stabilizing

effect on the growth rate in the Martian atmosphere results relative to the inclusion of these effects in air. The frequencies at which the largest growth rate occurs was also shown in these results. The peak nondimensional frequency is lower for the Martian case when including nonequilibrium thermodynamics, while the peak frequency does not shift as significantly for air. Although the disturbance environment is often uncertain, the difference in peak frequency has implications for the design of transition control, for example surface roughness. As illustrated in Figure 3, under assumptions of thermochemical nonequilibrium the boundary layer in the Martian atmosphere was more stable, and would likely transition later, as compared to air under the same freestream Reynolds number and Mach number on a flat plate under conditions where the 2nd Mack mode is dominant. This stabilizing effect was significant enough to require an alternate higher Reynolds number case in order to display meaningful stability results for the Martian atmosphere with thermochemical nonequilibrium. Under assumptions of finite-rate chemistry and neglecting thermal nonequilibrium, the opposite conclusion would be made. The reduced growth rates and N-factors encountered under thermochemical nonequilibrium in Martian atmosphere is corroborated by the stabilizing effect of CO_2 injection discussed in literature[31–33].

The destabilizing effect of finite-rate chemistry under these conditions is consistent with previous observations that endothermic chemical reactions and wall cooling are destabilizing to the 2nd Mack mode at hypersonic conditions, and the stabilizing effect of translational-vibrational relaxation is also consistent with literature. In the case investigated in this work, the latter effect appears to be dominant. This is likely to be sensitive to the model of vibrational-translational energy relaxation, and it may be possible that under other conditions - for example, including ablation products - the destabilizing effect of the endothermic chemical reactions would be more significant. These effects cannot be generalized to other flow conditions and other instability modes - systematic investigation of a range of instability modes and varied flow conditions is required to fully understand the effects of thermochemical nonequilibrium on boundary layers in either air or Martian atmosphere. The overall N-factors appear to be small for the flat plate configuration investigated. At a larger Reynolds number or higher temperature during reentry, more instability and higher N-factors should be expected.

Further application of these tools could be used to analyze boundary layer stability at conditions more closely related to planetary entry, and after development of a fully 3-dimensional version, it will also be possible to address a reentry geometry at an angle of attack. LASTRAC is already able to address 3-dimensional simulations for perfect gases only. The scenario included in this work is expected to be sensitive to the inclusion of ionic species, and comparisons between different chemical model assumptions. In order to account for the effects of ablation, the chemical composition of the ablation products, the mass flux of ablative products into the surrounding flow field, and the recession of the vehicle mold line would ideally be included, although the inclusion of all of these effects is beyond the capabilities of current tools. The recently-developed capabilities in LASTRAC are compatible with the addition of further chemical species, and initial steps have been taken toward accounting for the effects of ionization, however, these tools have not yet been applied. The critical N-factor is found empirically, and varies between flight and wind tunnel experiments due to the high disturbance amplitude usually found in wind tunnels. In order to determine a reasonable critical N-factor, quiet tunnel tests will be needed with CO_2 working gas. It may be possible to compare the transition locations found in previous Martian lander missions. It may also be possible to use N-factor predictions to either increase or decrease the chance of boundary layer transition through shape design coupled with N-factor predictions. This work focused on a case where the 2nd Mack mode was dominant. Blunt reentry vehicles are likely to encounter the 1st Mack mode as well as crossflow instabilities when at an angle of attack. These instability modes should be systematically investigated in the future, along with variations in the flow conditions.

Acknowledgments

This work was funded under NASA contract number NNL13A08B, task orders NNL17AA56T and 80LARC18F0084, supported by the Hypersonics Technology Project in the Aeronautics Mission Directorate. The authors would also like to thank Kyle Thompson, Bil Kleb, and Elizabeth Lee-Rausch for their help in editing and reviewing this paper.

References

[1] Hollis, B., Liechty, D., Wright, M., Holden, M., Wadhams, T., MacLean, M., and Dyakonov, A., "Transition Onset and Turbulent Heating Measurements for the Mars Science Laboratory Entry Vehicle," *43rd AIAA Aerospace Sciences Meeting and Exhibit, Aerospace Sciences Meetings*, (AIAA Paper 2005-1437), 2005. doi:10.2514/6.2005-1437.

[2] Edquist, K. T., Hollis, B. R., Johnston, C. O., Bose, D., White, T. R., and Mahzari, M., "Mars Science Laboratory Heat Shield

Aerothermodynamics: Design and Reconstruction," *Journal of Spacecraft and Rockets*, Vol. 51, No. 4, 2014, pp. 1106–1124. doi:10.2514/1.A32749.

[3] Chang, C.-L., Choudhari, M., Hollis, B., and Li, F., "Transition Analysis for the Mars Science Laboratory Entry Vehicle," *41st AIAA Thermophysics Conference*, (AIAA Paper 2009-4076), 2009. doi:10.2514/6.2009-4076.

[4] Johnson, H., Candler, G., and Wright, M., "Boundary Layer Stability Analysis of Mars Science Laboratory Aeroshell," *44th AIAA Aerospace Sciences Meeting and Exhibit*, (AIAA Paper 2006-920), 2006. doi:10.2514/6.2006-920.

[5] Saric, W. S., Reshotko, E., and Arnal, D., "Hypersonic Laminar-Turbulent Transition," *AGARD Advisory Report*, Vol. 2, 1998, pp. 2–2. URL `https://www.sto.nato.int/publications/AGARD/AGARD-AR-319-02/03chap02.pdf`.

[6] Bose, D., Brown, J. L., Prabhu, D. K., Gnoffo, P., Johnston, C. O., and Hollis, B., "Uncertainty Assessment of Hypersonic Aerothermodynamics Prediction Capability," *Journal of Spacecraft and Rockets*, Vol. 50, No. 1, 2013, pp. 12–18. doi:10.2514/1.A32268.

[7] Zanus, L., Miró Miró, F., and Pinna, F., "Nonlinear Parabolized Stability Analysis of Hypersonic Flows in Presence of Curvature Effects," *2018 AIAA Aerospace Sciences Meeting, AIAA SciTech Forum*, (AIAA Paper 2018-2087), 2018. doi:10.2514/6.2018-2087.

[8] Unnikrishnan, S., and Gaitonde, D. V., "Kovasznay-Type Analysis of Transition Modes in a Hypersonic Boundary Layer," *2018 AIAA Aerospace Sciences Meeting, AIAA SciTech Forum*, (AIAA Paper 2018-2086), 2018. doi:10.2514/6.2018-2086.

[9] Lakebrink, M. T., Paredes, P., and Borg, M. P., "Toward Robust Prediction of Crossflow-Wave Instability in Hypersonic Boundary Layers," *Computers & Fluids*, Vol. 144, 2017, pp. 1 – 9. doi:https://doi.org/10.1016/j.compfluid.2016.11.016.

[10] Moyes, A. J., Paredes, P., Kocian, T. S., and Reed, H. L., "Secondary Instability Analysis of Crossflow on a Hypersonic Yawed Straight Circular Cone," *Journal of Fluid Mechanics*, Vol. 812, 2017, pp. 370–397. doi:10.1017/jfm.2016.793.

[11] Kennedy, R. E., Laurence, S. J., Smith, M. S., and Marineau, E. C., "Visualization of the Second-Mode Instability on a Sharp Cone at Mach 14," *2018 AIAA Aerospace Sciences Meeting, AIAA SciTech Forum,*, (AIAA Paper 2018-2083), 2018. doi:10.2514/6.2018-2083.

[12] Miró Miró, F., Pinna, F., Beyak, E. S., Barbante, P., and Reed, H. L., "Diffusion and Chemical Non-Equilibrium Effects on Hypersonic Boundary-Layer Stability," *2018 AIAA Aerospace Sciences Meeting, AIAA SciTech Forum,*, (AIAA Paper 2018-1824), 2018. doi:10.2514/6.2018-1824.

[13] Knisely, C. P., and Zhong, X., "Supersonic Modes in Hot-Wall Hypersonic Boundary Layers with Thermochemical Nonequilibrium Effects," *2018 AIAA Aerospace Sciences Meeting, AIAA SciTech Forum,*, (AIAA Paper 2018-2085), 2018. doi:10.2514/6.2018-2085.

[14] Wang, X., "Passive Control of Hypersonic Non-Equilibrium Boundary Layers using Regular Porous Coating," *47th AIAA Fluid Dynamics Conference, AIAA AVIATION Forum*, (AIAA Paper 2017-4519), 2017. doi:10.2514/6.2017-4519.

[15] Wang, X., "Non-Equilibrium Effects on the Stability of a Mach 10 Flat-Plate Boundary Layer," *8th AIAA Theoretical Fluid Mechanics Conference, AIAA AVIATION Forum*, (AIAA Paper 2017-3162), 2017. doi:10.2514/6.2017-3162.

[16] Johnson, H., and Candler, G., "Hypersonic Boundary Layer Stability Analysis Using PSE-Chem," *35th AIAA Fluid Dynamics Conference and Exhibit, Fluid Dynamics and Co-located Conferences*, (AIAA Paper 2005-5023), 2005. doi:10.2514/6.2005-5023.

[17] Malik, M. R., "Hypersonic Flight Transition Data Analysis Using Parabolized Stability Equations with Chemistry Effects," *Journal of Spacecraft and Rockets*, Vol. 40, No. 3, 2003, pp. 332–344. doi:10.2514/2.3968.

[18] Chang, C.-L., Vinh, H., and Malik, M., "Hypersonic Boundary-Layer Stability with Chemical Reactions Using PSE," *28th Fluid Dynamics Conference, Fluid Dynamics and Co-located Conferences*, (AIAA Paper 1997-2012), 1997. doi:10.2514/6.1997-2012.

[19] Kline, H., Chang, C.-L., and Li, F., "Hypersonic Chemically Reacting Boundary-Layer Stability using LASTRAC," *2018 Fluid Dynamics Conference*, (AIAA Paper 2018-3699), 2018. doi:10.2514/6.2018-3699.

[20] Jaffe, R. L., Schwenke, D. W., Chaban, G. M., Prabhu, D. K., Johnston, C. O., and Panesi, M., "On the Development of a New Nonequilibrium Chemistry Model for Mars Entry," *55th AIAA Aerospace Sciences Meeting*, (AIAA Paper 2017-1372), 2017. doi:10.2514/6.2017-1372.

[21] Armenise, I., Reynier, P., and Kustova, E., "Advanced Models for Vibrational and Chemical Kinetics Applied to Mars Entry Aerothermodynamics," *Journal of Thermophysics and Heat Transfer*, Vol. 30, No. 4, 2016, pp. 705–720. doi:10.2514/1.T4708.

[22] Chaudhry, R. S., Singh, N., Grover, M. S., Schwartzentruber, T. E., and Candler, G. V., "Implementation of a Nitrogen Chemical Kinetics Model Based on ab-Initio Data for Hypersonic CFD," *2018 Joint Thermophysics and Heat Transfer Conference*, 2018. doi:10.2514/6.2018-3439.

[23] Bertolotti, F. P., "The Influence of Rotational and Vibrational Energy Relaxation on Boundary-Layer Stability," *Journal of Fluid Mechanics*, Vol. 372, 1998, pp. 93–118.

[24] Schneider, S. P., "Laminar-Turbulent Transition on Reentry Capsules and Planetary Probes," *Journal of Spacecraft and Rockets*, Vol. 43, No. 6, 2006, pp. 1153–1173. doi:10.2514/1.22594.

[25] Edquist, K., Liechty, D. S., Hollis, B. R., Alter, S. J., and Loomis, M. P., "Aeroheating Environments for a Mars Smart Lander," *Journal of Spacecraft and Rockets*, Vol. 43, No. 2, 2006, pp. 330–339. doi:10.2514/1.19431.

[26] Park, C., Howe, J. T., Jaffe, R. L., and Candler, G. V., "Review of Chemical-Kinetic Problems of Future NASA Missions. II - Mars Entries," *Journal of Thermophysics and Heat Transfer*, Vol. 8, No. 1, 1994, pp. 9–23. doi:10.2514/3.496.

[27] Kimmel, R., "Aspects of Hypersonic Boundary Layer Transition Control," *41st Aerospace Sciences Meeting and Exhibit, Aerospace Sciences Meetings*, (AIAA Paper 2003-772), 2003. doi:10.2514/6.2003-772.

[28] Whitehead, A., Jr., "NASP Aerodynamics," *National Aerospace Plane Conference, Meeting Paper Archive*, (AIAA Paper 1989-5013), 1989. doi:10.2514/6.1989-5013.

[29] Mack, L. M., "Boundary-Layer Linear Stability Theory," Tech. rep., California Institute of Technology Jet Propulsion Laboratory, 1984. URL `http://www.dtic.mil/docs/citations/ADP004046`.

[30] Chang, C.-L., "Langley Stability and Transition Analysis Code (LASTRAC) Version 1.2 User Manual," NASA TM- 2004-213233, NASA, Jun. 2004. URL `https://ntrs.nasa.gov/search.jsp?R=20040082550`.

[31] Jewell, J., Wagnild, R., Leyva, I., Candler, G., and Shepherd, J., "Transition Within a Hypervelocity Boundary Layer on a 5-Degree Half-Angle Cone in Air/CO2 Mixtures," *51st AIAA Aerospace Sciences Meeting Including the New Horizons Forum and Aerospace Exposition*, (AIAA Paper 2013-0523), 2013. doi:10.2514/6.2013-523.

[32] Wagnild, R., Candler, G., Leyva, I., Jewell, J., and Hornung, H., "Carbon Dioxide Injection for Hypervelocity Boundary Layer Stability," *48th AIAA Aerospace Sciences Meeting Including the New Horizons Forum and Aerospace Exposition*, (AIAA Paper 2010-1244), 2010. doi:10.2514/6.2010-1244.

[33] Leyva, I., Laurence, S., Beierholm, A., Hornung, H., Wagnild, R., and Candler, G., "Transition Delay in Hypervelocity Boundary Layers by Means of CO2/Acoustic Instability Interactions," *47th AIAA Aerospace Sciences Meeting including The New Horizons Forum and Aerospace Exposition*, (AIAA Paper 2009-1287), 2009. doi:10.2514/6.2009-1287.

[34] Candler, G. V., and Maccormack, R. W., "Computation of Weakly Ionized Hypersonic Flows in Thermochemical Nonequilibrium," *Journal of Thermophysics and Heat Transfer*, Vol. 5, No. 3, 1991, pp. 266–273. doi:10.2514/3.260.

[35] Anderson, J. D., *Hypersonic and High Temperature Gas Dynamics*, 2nd ed., AIAA education series, AIAA, Reston, Va, 2006. OCLC: 255373855.

[36] Thompson, R. A., Lee, K.-P., and Gupta, R. N., "Computer Codes for the Evaluation of Thermodynamic Properties, Transport Properties, and Equilibrium Constants of an 11-Species Air Model," NASA TM- 102602, NASA, 1990.

[37] McBride, B. J., Zehe, M. J., and Gordon, S., "NASA Glenn Coefficients for Calculating Thermodynamic Properties of Individual Species," NASA TP- 2002-211556, NASA, 2002.

[38] "Chemical Equilibrium with Applications," `https://www.grc.nasa.gov/www/CEAWeb/`, 2016 (last accessed 07/20/2018).

[39] Yos, J. M., "Transport Properties of Nitrogen, Hydrogen, Oxygen, and Air to 30,000 K," RAD TM- 63-7, AVCO Corp., 1963.

[40] Gupta, R. N., Yos, J. M., Thompson, R. A., and Lee, K.-P., "A Review of Reaction Rates and Thermodynamic and Transport Properties for an 11-Species Air Model for Chemical and Thermal Nonequilibrium Calculations to 30000 K," URL `https://ntrs.nasa.gov/search.jsp?R=19900017748`.

[41] Gnoffo, P. A., Gupta, R. N., and Shinn, J. L., "Conservation Equations and Physical Models for Hypersonic Air Flows in Thermal and Chemical Nonequilibrium," URL `https://ntrs.nasa.gov/search.jsp?R=19890006744`.

[42] Wright, M. J., Hwang, H. H., and Schwenke, D. W., "Recommended Collision Integrals for Transport Property Computations Part II: Mars and Venus Entries," *AIAA Journal*, Vol. 45, No. 1, 2007, pp. 281–288. doi:10.2514/1.24523.

[43] Park, C., "Assessment of Two-Temperature Kinetic Model for Ionizing Air," *Journal of Thermophysics and Heat Transfer*, Vol. 3, No. 3, 1989, pp. 233–244.

[44] Dunn, M. G., and Kang, S., "Theoretical and Experimental Studies of Reentry Plasmas," NASA CR- 2232, NASA, April 1973. URL https://ntrs.nasa.gov/search.jsp?R=19730013358.

[45] Millikan, R. C., and White, D. R., "Systematics of Vibrational Relaxation," *The Journal of Chemical Physics*, Vol. 39, No. 12, 1963, pp. 3209–3213.

[46] Park, C., "Problems of Rate Chemistry in the Flight Regimes of Aeroassisted Orbital Transfer Vehicles," *Progress in Astronautics and Aeronautics*, Vol. 96, 1985, pp. 511–537.

[47] Park, C., "Two-Temperature Interpretation of Dissociation Rate Data for N2 and O2," *26th Aerospace Sciences Meeting*, 1988, p. 458.

[48] Blottner, F. G., Johnson, M., and Ellis, M., "Chemically Reacting Viscous Flow Program for Multi-Component Gas Mixtures," SC-RR- 70-754, Sandia Labs., Albuquerque, NM, 1971. doi:10.2172/4658539, URL https://www.osti.gov/servlets/purl/4658539.

[49] Wie, Y.-S., "BLSTA: A Boundary Layer Code for Stability Analysis," NASA CR- 4481, NASA, 1992. URL https://ntrs.nasa.gov/search.jsp?R=19930005608.

[50] "VULCAN," http://vulcan-cfd.larc.nasa.gov/, 2016 (last accessed 02/07/2018).

[51] White, J. A. and Morrison, J. H., "Pseudo-Temporal Multi-Grid Relaxation Scheme for Solving the Parabolized Navier-Stokes Equations," *14th Computational Fluid Dynamics Conference*, (AIAA Paper 99-3360), 1999. doi:10.2514/6.1999-3360.

[52] Malik, M. R., and Anderson, E. C., "Real Gas Effects on Hypersonic Boundary-Layer Stability," *Physics of Fluids A: Fluid Dynamics*, Vol. 3, No. 5, 1991, pp. 803–821. doi:http://aip.scitation.org/doi/10.1063/1.858012.

[53] Hudson, M. L., Chokani, N., and Candler, G. V., "Linear Stability of Hypersonic Flow in Thermochemical Nonequilibrium," *AIAA Journal*, Vol. 35, No. 6, 1997, pp. 958–964. doi:10.2514/2.204.

[54] Stuckert, G., and Reed, H. L., "Linear Disturbances in Hypersonic, Chemically Reacting Shock Layers," *AIAA Journal*, Vol. 32, No. 7, 1994, pp. 1384–1393. doi:10.2514/3.12206.

[55] Johnson, H., and Candler, G., "PSE Analysis of Reacting Hypersonic Boundary Layer Transition," *30th Fluid Dynamics Conference, Fluid Dynamics and Co-located Conferences*, (AIAA Paper 1999-3793), 1999. doi:10.2514/6.1999-3793.